

Performances of a radial TPC for the detection of neutrinoless double beta decay

R. Bouet¹, J. Busto², A. Cadiou³, P. Charpentier¹, D. Charrier³, M. Chapellier⁴,
A. Dastgheibi-Fard⁵, F. Druillole¹, P. Hellmuth¹, C. Jollet¹, J. Kaizer⁸, I. Kontul⁸,
P. Le Ray³, M. Gros⁶, P. Lautridou^{b,3}, M. Macko⁷, A. Mereaglia^{a,1}, F. Piquemal¹,
P. Povinec⁸, M. Roche¹

¹LP2I Bordeaux, Université de Bordeaux, CNRS/IN2P3, F-33175 Gradignan, France

²CPPM, Université d'Aix-Marseille, CNRS/IN2P3, F-13288 Marseille, France

³SUBATECH, IMT-Atlantique, Université de Nantes, CNRS-IN2P3, France

⁴IJCLab, CNRS/IN2P3, Paris, France

⁵LPSC-LSM, CNRS/IN2P3, Université Grenoble-Alpes, Modane, France

⁶IRFU, CEA, Université Paris-Saclay, F-91191 Gif-sur-Yvette, France

⁷IEAP, Czech Technical University in Prague, CZ-11000 Prague, Czech Republic

⁸Faculty of Mathematics, Physics and Informatics, Comenius University, Bratislava, Slovakia

Received: date / Accepted: date

Abstract To search for $\beta\beta 0\nu$ decay with unprecedented sensitivity, the R2D2 collaboration is developing a radial time projection chamber with a fiducial mass of half a ton of ^{136}Xe at high pressure. The various approaches implemented to eliminate the radioactive background are presented in terms of detector design, topological recognition of interactions, and event energy reconstruction. The developed tools allow for the disentangling of the sought-after signal from the background, and the projected sensitivity after ten years of data taking yields a half-life limit exceeding 10^{27} years, along with a constraint on the effective neutrino mass $m_{\beta\beta}$, sufficient to exclude the inverted mass hierarchy region.

1 Introduction

The search for neutrinoless double beta decay ($\beta\beta 0\nu$) is essential for determining whether neutrinos are Dirac or Majorana particles, *i.e.* whether they are distinct from their antiparticles or identical to them. Identifying neutrinos as Majorana particles would imply lepton number violation, a critical feature in the leptogenesis theory, which explains the matter-antimatter asymmetry in the universe [1, 2]. $\beta\beta 0\nu$ is the only process that can confirm the Majorana nature of neutrinos, as it occurs only if the neutrino is its own antiparticle [3]. Additionally, detecting $\beta\beta 0\nu$ would provide insights into the absolute neutrino mass, an unresolved property of these particles. Thus, the search for this rare decay is pivotal for advancing both particle physics and cosmology.

Given the importance of such a potential discovery, the R2D2 (Rare Decays with Radial Detector) R&D program, initiated in 2017, has been developing a high-pressure, single-anode, radial Time Projection Chamber (TPC) specifically aimed at detecting $\beta\beta 0\nu$.

Experimentally, three key factors play a fundamental role in detector design: low background, large mass, and good energy resolution. Several ton-scale projects, such as LEGEND [4], CUORE [5], and nEXO [6], aim to achieve an effective Majorana neutrino mass, $m_{\beta\beta}$, of ~ 10 meV, which would rule out the inverted hierarchy region in the absence of any signals. Each technology has its own advantages but also presents some weaknesses. The R2D2 guideline has been to strike a balanced compromise, meeting all the critical requirements for the $\beta\beta 0\nu$ search simultaneously.

The energy resolution of a spherical TPC (SPC for Spherical Proportional Chamber) was the primary goal of the R2D2 R&D [7–10]. A cylindrical geometry (CPC for Cylindrical Proportional Chamber) was also studied and found to be an optimal solution when operated in the ionization regime [11]. It was demonstrated that a resolution of $\sim 1.2\%$ Full Width at Half Maximum (FWHM) could be achieved up to 10 bar with point-like and diffuse α sources of ~ 5.5 MeV, regardless of the gas used (argon or xenon).

In parallel, the issue of low background was addressed by minimizing the total material budget of the detector, a key concept of the proposed technology, which utilizes only one readout channel. A significant advancement was achieved through the use of a thin composite vessel to contain the pressurized gas. Ongoing studies on different carbon fibers and glues used to construct this gas tank are being conducted in collaboration with industry partners, (IRT Jules Verne [12]).

^ae-mail: anselmo.mereaglia@cern.ch

^be-mail: pascal.lautridou@subatech.in2p3.fr

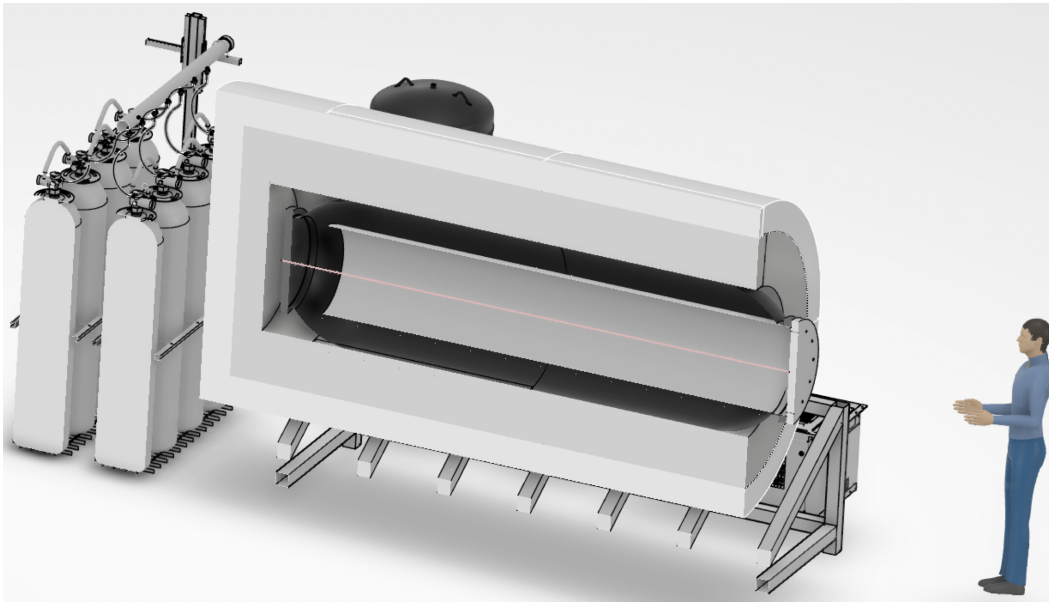


Fig. 1 Conceptual illustration of the detector setup.

The cylindrical active volume, which is 2.5 m long with a diameter of 1 m, can accommodate a usable xenon mass of 582 kg at 40 bars. Enclosed in a tank, this simple detection system could therefore be competitive with current ton-scale projects. The cost of the proposed detector should be much lower than that of currently identified experiments and would not require cryogenic infrastructure. Preliminary sensitivity studies on a spherical TPC were published in 2018 [13], demonstrating that, in principle, a background-free detector at the ton scale was feasible.

In the present work, a comprehensive sensitivity study of a ton-scale CPC is presented, based on the R&D results obtained over the last six years. A sensitivity on the half-life $T_{1/2}^{0\nu}$ greater than 10^{27} years can be achieved after ten years of data taking, corresponding to an effective neutrino mass $m_{\beta\beta}$ in the range of 5 to 21 meV.

2 Detector Setup

The detector geometry selected for the current sensitivity study is shown in the schematic view presented in Fig. 1. The main components are described below. The mechanical structure inherently minimizes the material budget, ensuring the lowest possible internal radioactivity. Although some elements, such as gas recirculation and purification, are not directly related to the detector simulation and do not affect the sensitivity study, all components are addressed for completeness.

– Central anode

The detector operates in ionization mode (*i.e.* without avalanche at the anode). For the current study, a copper

rod with a radius of 1 cm was chosen as the anode to model the collection of drifted electrons. However, in practice, a resistive anode will be used to exploit the charge sharing necessary for localization along the anode axis. The choice of radius is based on tests conducted on a previous CPC prototype, which demonstrated that a thick anode tube creates a higher drift field away from the anode, mitigating charge loss effects, and reduces geometrical distortions due to anode inhomogeneities. Improved energy resolution was indeed achieved with thick anodes in ionization mode [11, 14]. The anode is grounded and connected to the readout electronics at both ends. Grounding the anode and applying a negative high voltage to the cathode decouples the signal readout from the high voltage, thereby reducing electronic noise on the signal.

– Xenon volume

The tank, designed to withstand a maximum gas pressure of 60 bars, has a radius of 50 cm and a height of 350 cm, corresponding to a volume of 2.49 m^3 . This results in a xenon mass of 740 kg. By excluding the two rounded ends of the tank where the field is distorted (and where the anode is electrically masked), the active volume is reduced to the straight cylindrical section, which is 2.5 m high with diameter of 1 m. This corresponds to a useful volume of 1.96 m^3 and a ^{136}Xe mass of 582 kg at 40 bars.

– Xenon vessel

The xenon vessel design is based on the novelty of using composite materials. These materials consist of a mix of carbon fibers and epoxy glue. Composite tanks, few millimeter thick and withstanding pressures of several hundred bars, are already used today in space industry for

rocket fuel tanks and in the automotive industry for hydrogen reservoirs. The structure used in the present sensitivity study is made of 1.5 cm of carbon fiber-based composite material. This is very similar to the tank currently under test, produced by MAHYTEC company [15].

Dedicated studies are ongoing in cooperation with IRT Jules Verne company [12] to reduce the thickness and select low radioactivity materials. Several measurements of epoxy glues for low-background experiments have already been conducted [16], but no one has ever used carbon fibers in low radioactivity experiments. Carbon fibers are, in principle, relatively pure and radioactivity at the level of few μBq per kg can be achieved. However, they can become contaminated with uranium and thorium during the industrial sizing process, which prepares them for integration with the glue. Current measurements of carbon fibers and resins are being conducted in partnership with industry, aiming for a composite material with a radioactivity level of $10 \mu\text{Bq/kg}$.

A thin layer ($200 \mu\text{m}$) of aluminized mylar or another conducting material is deployed as a cathode on the inner side of the tank. This layer is polarized to a high voltage of -20 kV .

– Shielding

To shield the active volume from external radioactivity, a combination of lead and polyethylene surrounds the tank. Starting from the inside, a layer of 35 cm of lead is used primarily to block external gamma rays, accounting for a total mass of about 75 ton. An outer layer of 30 cm of polyethylene, designed to stop external neutrons, encloses the previous shell.

– Electronics

In the previous R&D prototype, the anodic signal was read only on one side by a charge amplifier: a custom-made amplifier for the proportional mode [7], and an ORTEC one for the ionization mode [11]. The waveforms were sampled at 2 MS/s by a CALI card (ADC), controlled by the SAMBA acquisition software [17]. In the present development, in order to achieve longitudinal localization, both sides of the anode must be grounded via specific amplifiers. These new devices (transimpedance ASIC amplifiers) are being developed based on SiGe technology. For the present simulation, to ensure our interpretation (in terms of noise and gain of the waveform), the amplifier outputs were modeled using the old response functions. The inducted current waveform was continuously sampled at 2 MHz , although a specific DAQ system is under development, allowing for more flexibility in the sampling frequency.

– Recirculation and purification

The gas purity in terms of electronegative contamination is critical to ensure long electron drifts and reduce attachment, which impacts the final signal integral and, there-

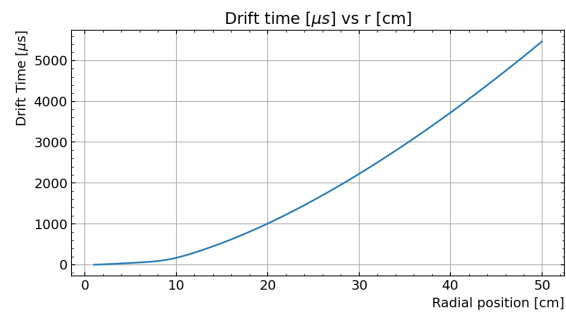


Fig. 2 GARFIELD++ simulation of the drift time as a function of the radial position for a cathode of 50 cm at -20 kV and a central grounded anode with a radius of 1 cm. The CPC is filled with xenon gas at 40 bar.

fore, the energy resolution. For the R&D, a system of hot and cold getters was used together with a recirculation piston pump. A purity allowing for an electron lifetime of $\sim 2 \text{ ms}$ was achieved at 10 bar [11], which is a factor of 5 worse than what is currently achieved in liquid xenon experiments [18]. The system used was also limited in terms of gas flow (10 l/min) and maximum operating pressure (10 bar). For the proposed detector, the existing technology developed for noble liquid gas detectors could be used (*i.e.* cryogenic filters built from copper [18] or the spark discharge techniques [19]), granting a sufficiently pure gas to operate the proposed technology with a detector having the planned radius of 50 cm. The recirculation pump, a source of electronegative impurities, will also be replaced by a magnetically driven piston pump [20].

To install the detector in an underground laboratory, a footprint of approximately 50 m^2 is required to ensure safe operation of the detector and the recirculation/recuperation system. The estimated cost of the full detector, excluding the cost of xenon gas, is projected to be well below 5 M€ .

3 Signal waveform construction

The sensitivity study relies on the detector simulation tools that were developed based on the best existing knowledge, exploiting the results of the detector response recorded during the entire R2D2 R&D.

The physics simulation relies on GEANT4 [21]: for all particles (signal and background) traversing the active volume, the energy deposits were saved. For each deposit, the position and the released true energy were recorded, forcing a step size of $100 \mu\text{m}$. The second step of the simulation involves constructing the registered waveform based on the GEANT4 information. To do this, the procedure is divided into three steps:

- The energy deposited is converted into a number of ionisation electrons that are then drifted to the anode. This conversion is achieved by dividing the deposited energy

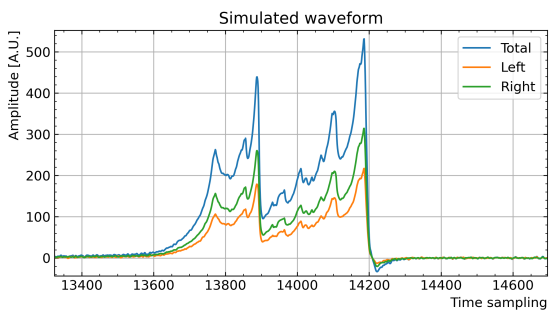


Fig. 3 Example waveform of a $\beta\beta 0\nu$ events starting at a radial position of 26.5 cm and a longitudinal position of $Z=139$ cm.

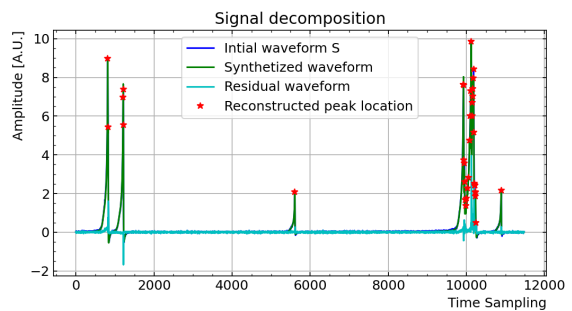
by the energy required to create an electron-ion pair (*i.e.* the so-called W_i), which is 22 eV in xenon [22]. An integer number of electrons is assumed, although no additional smearing or quenching are accounted for. Previous studies on quenching [22] suggests indeed that it can be neglected, whereas energy smearing based on experimental results will be applied at the analysis level (see Sec. 5).

- Using a GARFIELD++ [23] simulation of the detector geometry, the electron drift time to reach the anode is computed for each energy deposit and used to construct the waveform. A high voltage of -20 kV is applied to the cathode at a radius of 50 cm, while the central anode with a radius of 1 cm is grounded. The resulting drift time as a function of the starting electron radial position is shown in Fig. 2. Validation of the GARFIELD++ simulated drift time against data was performed as part of the R&D work, demonstrating reasonable agreement [24].
- Based on the Shockley-Ramo theorem (see Ref. [11] for details), two partial waveforms are reconstructed for each energy deposit: S_l for the left side and S_r for the right side of the anode. These two time series originate from the same initial partial waveform S_i , which is truncated according to the position R of the deposit. However, their amplitudes differ depending on the charge distribution, which is affected on the longitudinal position Z of the deposit in the simulation. Assuming an anode resistance of several $k\Omega$, amplifier input impedances of the order of Ω [25], and taking $Z = 0$ at the left edge of the detector, they conform to the following relationships:

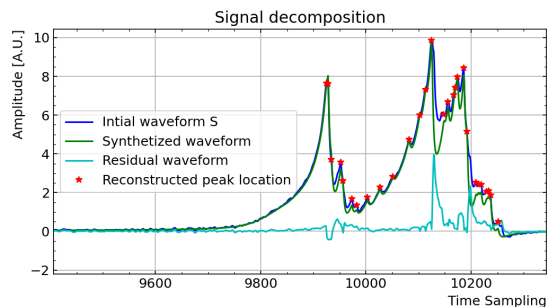
$$S_l = S_i \times (1 - Z/Z_{det}) \quad (1)$$

$$S_r = S_i \times (Z/Z_{det}) \quad (2)$$

where S_i represents the partial waveform without charge-sharing effect (*i.e.* $S_i = S_l + S_r$), Z is the GEANT4 hit position along the anode axis, and Z_{det} is the total anode length (2.5 m). After adding all partial contributions from energy deposits, a convolution with an electronic response and filtering is applied. To mimic real noise, noisy snapshots based on data are independently added



(a)



(b)

Fig. 4 Example of the decomposition of the total signal S from a single event of ^{208}Tl produced by the ^{232}Th decay chain simulation. The full waveform is shown in Fig. 4(a), while a zoomed-in view is presented in Fig. 4(b). The blue line indicates the original waveform, the green line shows the decomposition result, and the cyan curve displays the residue of the decomposition. The red stars mark the maxima of the different elementary contributions identified by the decomposition algorithm.

to S_l and S_r . These time series were extracted from the measurements presented in Ref. [11]. To reflect real conditions, the true total signal S , used later in the analysis, is then constructed by summing S_l and S_r , which contain uncorrelated noise sequences.

An example of the waveform of a $\beta\beta 0\nu$ event is shown in Fig. 3.

4 Waveform analysis

Once the anodic signals have been generated, it is necessary to develop a method for analyzing them. Following the procedure developed in previous works [11], some global observables can be derived using the total waveform S , namely:

- The total reconstructed charge Q_r . An overall calibration is performed to align the peak of $\beta\beta 0\nu$ events corresponding to the expected $Q_{\beta\beta}$ of 2.458 MeV.
- The total signal duration D_t .

The analysis of the internal modulation of the signals can be performed to recover the radial and longitudinal location of the energy deposits, and thus reconstruct the particle track

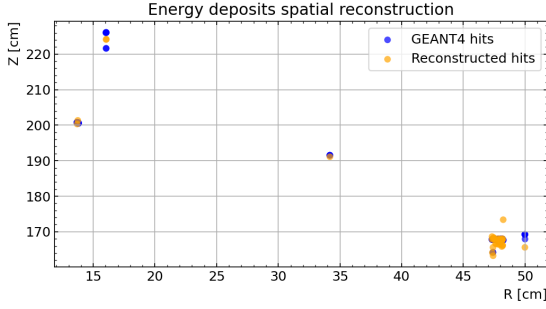


Fig. 5 Reconstruction of the elementary interactions (orange points) for the same ^{208}Tl event shown in Fig. 4, in the natural (R, Z) plane as induced by the radial TPC. The blue points correspond to the original GEANT4 hit locations.

inside the gas. By analysing the different peaks, it is possible to reconstruct the radial position R via the drift time and the longitudinal position Z via the amplitude ratio of S_l and S_r . Furthermore, a finer decomposition of the total signal S into elementary contributions could be considered. This was carried out (see Fig. 4) by a simple iterative method of signal synthesis, where the process is interrupted when $Q_{\text{synthesized}}/Q_r > 0.99$. As a result, it was possible to create a more detailed map of the interaction footprint in the (R, Z) plane (see Fig. 5), with an accurate estimate of the initial primary charge for each GEANT4 hit being also a by-product of the routine.

Ultimately, this approach allows the extraction of the following ancillary observables, which have been used for further analyses:

- The number of peaks in the waveform N_p . As explained before, for each peak, the radial position is reconstructed based on its drift time, and its Z position is determined from the ratio between the left and right waveforms.
- The event radial elongation ΔR is computed as the maximal distance between the radial positions of the individual peaks.
- The event longitudinal elongation ΔZ along the Z axis corresponds to the maximal distance between the Z positions of the individual peaks.
- The largest radial position of the reconstructed peaks, denoted as $MaxR$.

Associated with specific cuts discussed in Sec. 6, these estimators play a key role in distinguishing the topology of the $\beta\beta 0\nu$ signals from the background. The quality of the localization of the interactions was estimated by comparing the barycenters in R and Z (computed using the charge of the deposits as weight) for the GEANT4 events with those reconstructed by our processing. The distributions of the residuals are presented in Fig. 6).

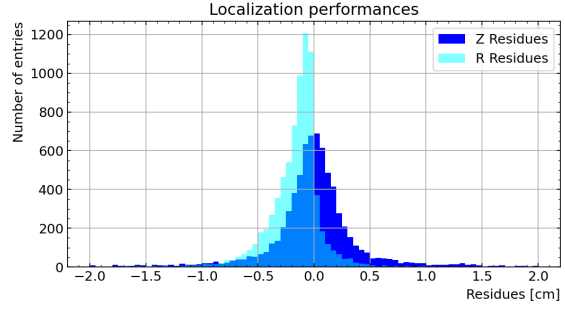


Fig. 6 Residual distributions in R and Z for the simulated signal interactions, including satellite deposits resulting from the multiple interactions in the gas.

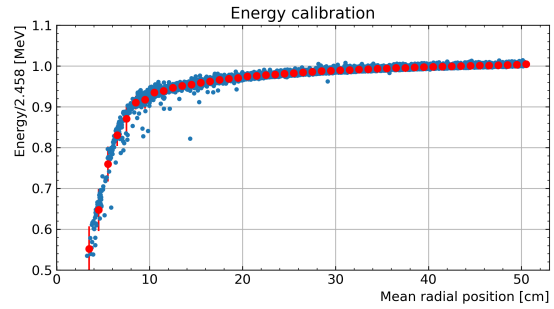


Fig. 7 Fraction of energy with respect to the $Q_{\beta\beta}$ as function of the event mean radial distance (weighted by the charge for the different energy deposits). The red points represent the mean values with steps of 1 cm.

5 Energy reconstruction

Energy reconstruction is critical as it directly impacts event selection and the definition of the so-called ROI (*i.e.* Region Of Interest).

As mentioned in Sec. 4, the waveform integral is normalised to match the signal $Q_{\beta\beta}$; however, the reconstructed charge depends on the radial position of the energy deposit, since only drifted electrons contribute to the observed signal, while ions are below the noise level due to their low mobility (see Ref. [11] for more details). For this reason, the true energy must be estimated relative to a common reference, by correcting the deficit associated with charge produced at radial position R compared to that at the cathode. Two correction strategies were developed:

- The reconstructed energy as a function of the radial position was simulated for $\beta\beta 0\nu$ events. This robust approach is based on a correction of the signal integral as a function of the mean radial distance R of the trace. As illustrated in Fig. 7, where the red dots represent the mean values in 1 cm intervals, a linear interpolation between these points is used to derive a corrective function, which calibrates the apparent energy as a function of the radial position R of the events.

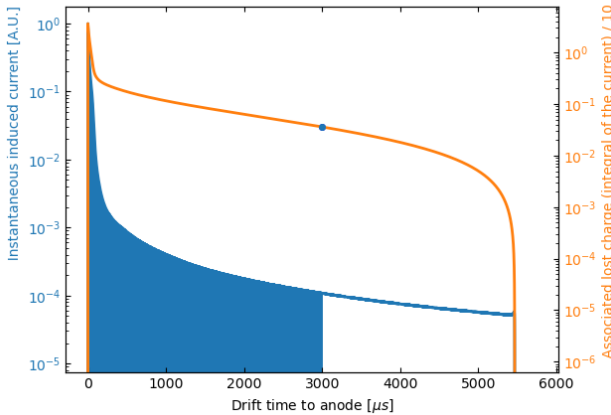


Fig. 8 Instantaneous current (blue) induced by an elementary charge and corresponding lost charge (orange) as a function of the drift time. For illustration, the marker indicates the energy lost associated with a primary created at $R = 35.38$ cm, and the corresponding waveform is shown by the blue area.

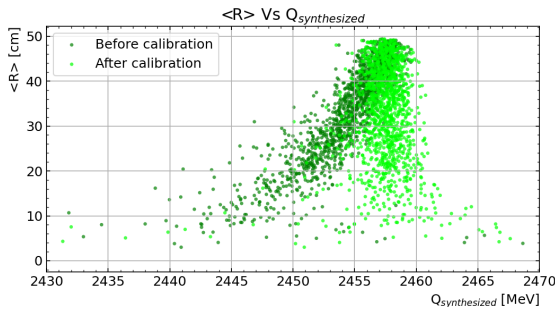


Fig. 9 Reconstructed charge $Q_{\text{synthesized}}$ of simulated $\beta\beta 0\nu$ events using the synthesis method as a function of the signal mean radial position R before and after the calibration procedure explained in the text.

- The synthesis method also allows calculation of the reconstructed energy deficit. For each cluster of an event, identified by the decomposition algorithm at a given radial position R (*i.e.* at a given drift time), the energy deficit is determined by multiplying the value of the lost charge function at that position by the number of primaries estimated at the same point. Summing over the different clusters enables the correction of the energy deficit due to the varying initial radial positions of the primaries in the event (see Fig. 8).

Although the synthesis method does not require additional calibration in principle, a weak radial dependence was still observed in the identification diagram ($Q_{\text{synthesized}}$, R) (see Fig. 9). This phenomenon can be attributed to errors in defining the signal origin (*i.e.* when the signal crosses the threshold), which are influenced by noise and have a more significant impact when the signal originates near the anode, where the signal slope is steeper. Therefore, a second corrective step was implemented, utilizing the previously described

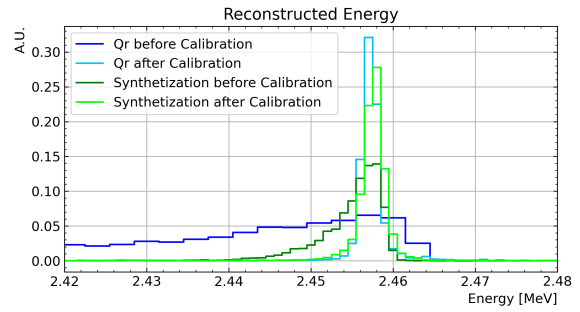


Fig. 10 Energy reconstructed by integrating the simulated signal waveform of $\beta\beta 0\nu$ events before (blue line) and after (cyan line) the calibration procedure. The results after the waveform synthesis are also shown, both before (green line) and after (light green line) the calibration procedure.

method applied to the signal integral, to further enhance the calibration.

Given the dependence of the signal on the radial position R , an experimental energy calibration of the detector must be conducted. Two possible solutions are currently being studied. The first option involves using a dedicated point-like alpha source deployed at specific radial positions, though this could potentially disturb the drift electric field. Another attractive solution is to exploit the diffuse radon dissolved in the gas, as it likely constitutes an ultimate and irreducible background.

The energies reconstructed before and after the calibration procedures previously discussed are shown in Fig. 10. A Gaussian fit of the distribution obtained after energy correction shows a resolution of 0.1% FWHM for both methods. Although both approaches yield similar results, the synthesis routine is deemed more satisfactory from a methodological perspective. Consequently, this method was used for energy estimation in this article.

To perform a realistic sensitivity study, the energy resolution must account for additional uncertainties. At this stage, effects due to fluctuations in the number of electrons or charge loss from attachment to gas impurities during drift have not been included. A separate statistical error of 0.3% FWHM is expected, assuming a Fano factor of approximately 0.15 [26]. Additionally, for real data, the influence of front-end electronics (amplifier response function) or digital processing (time shift of the sampling comb between the two ADCs) can also affect the energy resolution.

Previous experimental work on proportional parallel projection chambers achieved a resolution of 0.7% FWHM at 660 keV [27]. When rescaled as $1/\sqrt{E}$ to the xenon $Q_{\beta\beta}$, this corresponds to a resolution of 0.4% FWHM, close to the statistical limit. Experimental results from the R2D2 CPC showed an energy resolution of 1.2% FWHM at 5.3 MeV [11]. Optimised analysis based on the signal processing discussed in Sec.4 enabled a resolution of 0.7% FWHM at 5.3 MeV, which corresponds to 1% FWHM at the xenon $Q_{\beta\beta}$, the orig-

inal goal of the R2D2 R&D. The factor-of-two difference compared to Ref. [27] can be attributed to the experimental results being dominated by electronic noise and gas quality. Future experimental results are expected to improve significantly with better noise conditions, upgraded electronics and better-purified gas.

To account for the aforementioned uncertainties, an energy resolution of 1% FWHM at the xenon $Q_{\beta\beta}$ is conservatively chosen for the following sensitivity study. Consequently, the reconstructed energy of each event is spread using a Gaussian function, where the width corresponds to this assumed final energy resolution.

6 Selection cuts

The first selection is based on the event's reconstructed energy, considering only those events that fall within the defined ROI. This ROI selection is closely related to the achieved energy resolution, and previous studies have shown that an ROI with a half-width equal to the energy resolution, expressed as FWHM, is the optimal choice [13]. Given the assumed energy resolution of 1% (see Sec. 5) at the xenon $Q_{\beta\beta}$, this translates to an ROI in the range of [2.433 – 2.483] MeV.

Additional selection cuts are based on the observables built from the reconstruction. They are tuned to reduce the background in the ROI as much as possible while keeping the signal acceptance at a reasonable level of at least $\sim 60\%$. The distributions of these observables, associated with the typical cuts used for the $\beta\beta 0\nu$ signal and the main background components, are shown in detail in Fig. 11. The selections on the different variables are detailed below with an explanation of the logic behind each choice. It is important to note that, at this level, the geometric reconstruction of events depends only weakly on the energy resolution, despite the presence of smearing.

A first source of background originates from α 's or β 's arriving from the vessel or from outside. To mitigate this background, a selection requiring $MaxR$ to be smaller than 49 cm is applied, removing events with energy deposits in the outermost centimeter of the active volume.

A second source of background arises from γ 's interacting within the active volume and depositing energy within the accepted ROI. However, these events typically undergo multiple Compton interactions, resulting in a topology that is less compact compared to the expected signal electron tracks. Multiple spatial cuts demonstrated effective background rejection, namely $\Delta R < 4$ cm, $\Delta Z < 14$ cm, and $\Delta R \times \Delta Z < 30$ cm². Additionally, these events exhibit a large number of reconstructed peaks, prompting the application of a cut on $N_p < 25$.

7 Signal simulation

To simulate the signal, *i.e.* the two electrons emitted in the $\beta\beta 0\nu$ decay, pre-computed spectra were used [28], as this decay is not included in GEANT4. The angular correlation between the two electrons was not considered, but its impact is expected to be a second-order effect.

The events are simulated isotropically throughout the xenon volume, but only events generated in the active volume (*i.e.*, about 75% of the total events) are used to estimate the detection efficiency. The breakdown of selection efficiencies after the various selection steps can be found in Tab. 1, resulting in a final signal selection efficiency of 61%.

Events in ROI	+ Topology cuts
82.2%	60.8%

Table 1 Fraction of signal in the ROI without and with topological selection cuts.

8 Background simulation

8.1 $\beta\beta 2\nu$

The high-energy tail of events from the $\beta\beta 2\nu$ process could contribute to background if it falls within the ROI, as these events would be indistinguishable from the sought-after signal. Assuming a 582 kg mass of pure ¹³⁶Xe (see Sec. 2) and a mean lifetime $T_{1/2}^{2\nu}$ of 2.165×10^{21} years [29], the total expected number of decays per year is approximately 825000. Considering an ROI of [2.433 – 2.483] MeV, and accounting for 1% FWHM energy smearing at the xenon $Q_{\beta\beta}$ of 2.458 MeV, only a fraction of 9×10^{-10} events would fall in the ROI. This corresponds to less than 0.001 events per year, allowing this background source to be completely neglected.

8.2 Composite material radioactivity

A specific composite material selection process is currently underway in collaboration with the IRT Jules Verne company. Various carbon fibres are being evaluated based on their radioactivity and mechanical strength to withstand pressure, alongside different epoxy glues to bind them. As mentioned in Sec. 2, a structure with a 1.5cm thick carbon fibre-based composite material has been assumed. The decay chains of ²³⁸U and ²³²Th, as well as ⁶⁰Co decays, were simulated uniformly within the carbon fibre layer. For the sensitivity studies, it was assumed that material radioactivity at the level of 10 μ Bq/kg can be achieved. While this remains a critical point yet to be fully demonstrated, promising results

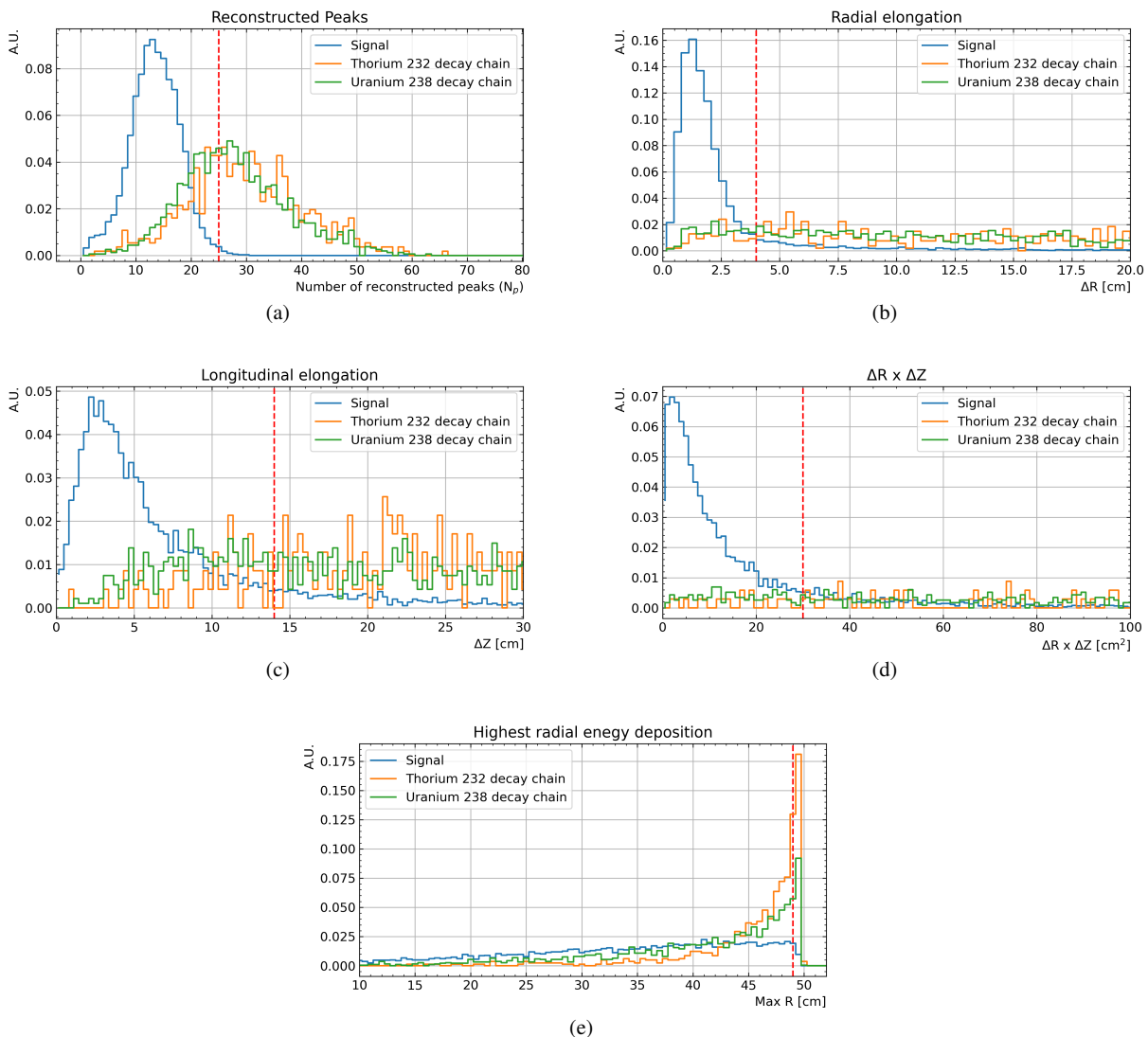


Fig. 11 Selection cuts, indicated by the vertical red dashed line, on several observables, namely: number of reconstructed peaks 11(a), ΔR 11(b), ΔZ 11(c), $\Delta R \times \Delta Z$ 11(d), and larger radial energy deposit position 11(e). The distribution of such observables (after ROI selection) for $\beta\beta 0\nu$ (blue), Thorium 232 chain (orange) and Uranium 238 chain (green) are shown.

have been obtained through the partnership with IRT Jules Verne. In any case, the presented background event rates per year can be scaled linearly with respect to different material radioactivity levels.

In the GEANT4 simulation, a conservative time window of 10ms was assumed to separate events in the decay chain, considering a maximal drift time of approximately 5ms. Given the half-lives of 164 μs for ^{214}Po (from the ^{238}U chain) and 300 ns for ^{212}Po (from the ^{232}Th chain), Bi-Po decays are treated as a single event in the detector simulation. For each decay chain, a sample of 10 million events was simulated. Only events depositing more than 2.2 MeV in the xenon active volume at the GEANT4 level were further processed. Based on the assumed activity of 10 $\mu\text{Bq/kg}$

and the composite mass of approximately 330 kg, the generated statistics correspond to about 10 years of data for ^{232}Th , 7 years for ^{238}U , and 90 years for ^{60}Co .

The total number of expected events per year in the ROI, before any selection cuts, can be computed, as well as the irreducible background events surviving the selection cuts described in Sec.6. A summary is presented in Tab. 2, which shows that the total number of background events from the composite vessel's radioactivity is approximately 1.3 per year. All the selected events in the ^{232}Th decay chain originate from ^{208}Tl decays, while the events from the ^{238}U decay chain are from ^{214}Bi decays. In both cases, a γ deposits all the energy in a confined region of the detector, with no multi-Compton topology to enable event rejection.

Source	Events in ROI	+ Topology cuts
^{60}Co	217.7	0.1
^{232}Th	80.5	0.5
^{238}U	25.8	0.7
Total	324.0	1.3

Table 2 Background events per year in the ROI, before and after applying topological selection cuts.

8.3 External gammas

The background due to external gamma radiation is strongly dependent on the detector's location. In the present study, the assumed gamma spectra and rate are based on measurements performed at the underground laboratory in Modane (LSM) [30]. Following the same strategy as in Ref. [13], the gamma spectra are divided into three energy ranges: 1-4 MeV, which primarily includes gammas from natural radioactivity; 4-6 MeV, which accounts for gammas emitted by the detector itself; and 6-10 MeV, which comprises gammas resulting from neutron capture in the surrounding materials.

The expected gamma flux in the 1-4 MeV region is 0.12 events $\text{cm}^{-2} \text{s}^{-1}$. Gammas were generated in the GEANT4 simulation within a sphere of 280 cm radius, homogeneously and isotropically, resulting in a statistic of approximately 3.7×10^{12} events per year. The total simulated statistics is 4×10^{13} events, corresponding to more than 10 years of data. Out of this total, 1 event remains after cuts, leading to an expected background of 0.1 events per year. This background can, of course, be reduced by increasing shielding if necessary.

Gammas with energies between 4 and 6 MeV are predominantly due to the detector used for the measurement; therefore, the extrapolation from the LSM measurement (considered as an example of a potential underground laboratory location) to the present sensitivity study may be affected by significant uncertainties. Considering the measured flux of 3.8×10^{-6} events $\text{cm}^{-2} \text{s}^{-1}$ and the simulated statistics of 1×10^{10} events, generated on the same spherical surface used for the low-energy gammas, this corresponds to a period of over 80 years. Since no events survive the selection cuts, an upper limit can be computed. The upper bound of a 90% confidence level (C.L.) interval for a Poisson signal mean, when 0 events are observed, is 2.44 [31], leading to an upper limit of approximately 0.03 events per year.

The last energy region studied is between 6 and 10 MeV, corresponding to gammas emitted from nuclear radiative capture in the materials constituting and surrounding the detector. The measured flux at LSM was 3.2×10^{-6} events $\text{cm}^{-2} \text{s}^{-1}$, resulting in an upper limit of 0.02 events per year, considering the simulated statistics of 1×10^{10} events and no events passing the topological selection cuts. All the results are summarized in Tab. 3.

Energy	Events in ROI	+ Topology cut
1-4 MeV	2.9	0.1
4-6 MeV	0.03	< 0.03
6-10 MeV	< 0.02	< 0.02
Total	2.9	0.1

Table 3 Gamma background per year in the ROI, without and with topological selection cuts.

8.4 External neutrons

Neutrons emitted from radioactive decays or (α ,n) reactions in the laboratory environment surrounding the detector, as well as neutrons produced by cosmic muon spallation reactions, could be sources of background. Several specific neutron-related backgrounds are considered below.

- *Neutron captures on detector materials*
Neutron captures on materials such as Pb, Cu, or Fe produce high-energy gammas in the energy region between 6 and 10 MeV. These gammas have already been considered in the external gamma section (*i.e.* Sec. 8.3).
- *Neutrons produced inside the detector by cosmic muons*
Neutrons generated by muons inside the detector can be easily tagged, as the muon deposits a significant amount of energy in the active volume. The only potential issue is deadtime (addressed in Sec. 9), but this is negligible given the extremely low muon rate at underground laboratories (*e.g.* $4 \text{ m}^{-2} \text{ day}^{-1}$ at LSM).
- *Neutron captures on xenon*
Neutrons entering the detector can be captured by xenon, resulting in the emission of several gammas with a total energy of a few MeV. The expected neutron flux of 4×10^{-6} events $\text{cm}^{-2} \text{s}^{-1}$ and the energy spectrum between 2 and 6 MeV were obtained from measurements performed at LSM [30]. Similar to the gamma simulation, neutrons were generated in the GEANT4 simulation on a sphere with a radius of 280 cm, homogeneously and with isotropic directions, yielding a statistics of about 1.2×10^8 events per year. GEANT4 was also used to estimate neutron captures on the ^{136}Xe isotope. The simulated statistics of 3×10^{10} events, corresponding to approximately 240 years of data taking, a the total number of background events after cuts of 0.02.
- *Spallation neutrons*
The energy of spallation neutrons can reach several GeV, and the induced nuclear recoils may produce signals in the ROI that are difficult to reject. The neutron energy spectrum from Ref. [32] was used in the simulation, assuming a flux above 10 MeV of 5×10^{-10} events $\text{cm}^{-2} \text{s}^{-1}$, based on an underground depth of 4800 m.w.e., corresponding to that of LSM. A total of 1×10^6 events

was simulated (approximately 64 years of data taking), yielding an expected rate of 0.02 events per year.

The neutron related background expectation is summarized in Tab. 4

Source	Events in ROI	+ Topology cut
Capture on ^{136}Xe	6.7	0.02
Spallation neutrons	3.7	0.02
Total	10.4	0.04

Table 4 Neutron background per year in the ROI, without and with topological selection cuts.

8.5 Radon

Radon is one of the ultimate sources of background in low-radioactivity experiments. Cryogenic distillation is an effective method for radon removal [33], and the nEXO collaboration aims to reach a contamination limit of $0.3 \mu\text{Bq/kg}$ [34]. However, maintaining 1 ton of xenon at this low contamination level during data collection requires 1 ton of liquid nitrogen daily. Although radon's molecular size is similar to that of xenon, complicating its capture using standard molecular filters, ongoing research explores alternative absorbers [35].

A sample of 1×10^7 radon events was simulated homogeneously in the xenon volume, and the full digitization and analysis chain was applied to the Monte Carlo events. A rejection factor of 3×10^{-7} was achieved after cuts. Assuming a radon activity level of $5 \mu\text{Bq/kg}$ (corresponding to 1.5 mBq/m^3), a conservative estimate relative to the contamination levels expected in xenon experiments ($0.3 \mu\text{Bq/kg}$ for nEXO [34], $1 \mu\text{Bq/kg}$ for XENONnT [36], and $3.5 \mu\text{Bq/kg}$ for PandaX-4T [37]), the resulting background amounts to about 0.2 events per year.

8.6 Cosmogenic background

Cosmogenic nuclei produced by muons passing through the xenon volume could contribute to the background, as these nuclei may undergo beta decays, potentially yielding signals in the ROI. A detailed simulation by the EXO-200 collaboration [38] identified ^{137}Xe as the primary contributor to signals near the ^{136}Xe $Q_{\beta\beta}$. The production rate of ^{137}Xe depends on both the muon flux and their energy.

Comprehensive studies have been conducted for natural xenon [39] and enriched ^{136}Xe [40] at different underground sites. Assuming a detector filled with enriched ^{136}Xe , which results in higher ^{137}Xe production, the expected rate at LSM is conservatively estimated to be $1.3 \times 10^{-2} \text{ kg}^{-1} \text{ year}^{-1}$.

This value was derived from studies at SURF (4300 m.w.e.), which has a lower depth than LSM (4800 m.w.e.), and corresponds to an expected production rate of approximately 10 events per year in the proposed setup. Given a selection efficiency of 1.6×10^{-4} , determined from the full simulation chain, this background source can be considered negligible.

8.7 Background summary

Various potential sources of background were considered for the proposed detector. Assuming the CPC is filled with pure ^{136}Xe and situated underground at 4800 m.w.e. (the depth of LSM), the expected background level is approximately 1.6 events per year. This estimate may vary slightly depending on the specific underground laboratory, influenced by differences in overburden and environmental radioactivity. However, the result is valid for similar sites, such as LNGS in Italy. A summary of the background contributions after selection cuts is provided in Tab. 5, where a 90% confidence level upper limit is used in cases where no events passed the cuts in the simulation.

Contribution	Events per year
$\beta\beta 2\nu$	1.0×10^{-3}
Composite radioactivity	1.3
External gammas	0.1
External neutrons	0.04
Radon	0.2
Cosmogenic background	1.6×10^{-3}
Total	1.6

Table 5 Summary of background contributions after selection cuts.

9 Pile Up

The total event rate is a critical parameter for the experiment. Given the long drift time, on the order of a few milliseconds, even events outside the ROI, though not directly contributing to the background, could overlap with good events, compromising their energy or position reconstruction. To maintain a minimal pile-up probability of 5×10^{-3} , assuming a time window of 5 ms which corresponds to the maximum expected drift time, the event rate should be kept below 1 Hz. The same background sources considered in Sec.8 were re-evaluated with a significantly lower energy threshold, down to a few keV.

As computed in Sec. 8.1, the number of $\beta\beta 2\nu$ events expected per year is approximately 825000, corresponding to an event rate of $\sim 0.03 \text{ Hz}$.

The radioactivity of the composite material was simulated in Sec. 8.2, focusing on ^{60}Co , ^{232}Th , and ^{238}U , with an assumed activity of $10 \mu\text{Bq/kg}$. The fraction of events releasing energy within the xenon active volume is 43%, 8%, and 5%, respectively. Based on the expected number of events, the rates for these decay chains are 1.4×10^{-3} Hz, 2.2×10^{-3} Hz, and 2.2×10^{-3} Hz, yielding a total rate of 5.8×10^{-3} Hz.

The external gamma simulation from Sec. 8.3 was used to calculate the fraction of events depositing energy in the active volume. Out of 1×10^8 simulated events between 1 and 4 MeV, only one event deposited energy in the xenon active volume. Scaling this fraction to the expected number of events per year yields an event rate of 1.2×10^{-3} Hz. For the 4 to 6 MeV and 6 to 10 MeV ranges, no events deposited energy in the active volume within the simulated 1×10^7 events. This results in an upper limit of approximately 29 and 24 events per year, respectively, corresponding to a negligible rate of $\sim 1 \times 10^{-6}$ Hz in both cases.

The external neutrons were discussed in Sec. 8.4. A total of 1×10^6 events were generated, with a fraction of $\sim 1.4 \times 10^{-4}$ producing a signal inside the detector. Based on the expected neutron flux per year, this contribution results in a trigger rate of approximately 5×10^{-4} Hz. The contribution from spallation neutrons is significantly smaller, given that the expected flux is lower by four orders of magnitude. Despite a fraction of events inducing a signal at the level of 5×10^{-2} , the resulting rate is 2.5×10^{-5} Hz.

Radon background was discussed in Sec. 8.5, where an activity level of $5 \mu\text{Bq/kg}$ was assumed. With 76% of events producing a signal in the active volume, this corresponds to approximately 617000 events per year, resulting in a rate of 0.02 Hz.

Finally, the cosmogenic background discussed in Sec. 8.6 must be considered. For pile-up studies, the relevant factor is the number of muons crossing the detector rather than the isotopes produced. Using the expected muon rate at LSM of $4\text{m}^{-2} \text{day}^{-1}$ and conservatively assuming a circular surface above the detector with a 10 m radius (i.e., muons with zenith angles up to 80 degrees), approximately 1256 muons per day are expected. If all of these muons are assumed to pass through the detector, the resulting rate is 0.015 Hz.

Additionally, an extra source of pile-up could arise from ^{40}K contamination in the composite material. Although this source was not studied in the background section, as the maximum energy released in the decay (1.5 MeV) is outside the ROI, ^{40}K contamination in glass is a known issue in experiments using photomultiplier tubes for signal detection. It should therefore also be considered in composite materials. The fraction of simulated events depositing energy in the xenon volume is 3.7%. No direct measurements have yet been performed on the composite materials proposed for the tank, so the contamination level was estimated based on glass

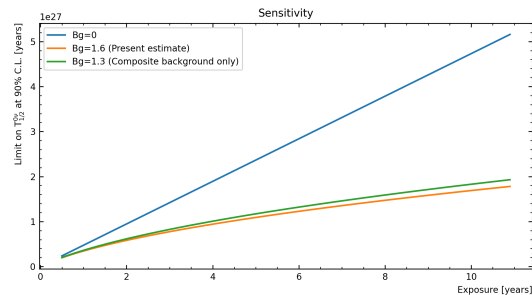


Fig. 12 Expected sensitivity at 90% C.L. for zero background (blue line), for the expected background of 1.6 events per year (orange line), and for the contribution due to composite radioactivity only (green line).

measurements [41]. Assuming an activity of 1 mBq/kg , the expected rate is 0.12 Hz , representing the largest contribution to the pile-up.

The total event rate expected in the detector is approximately 0.19 Hz (see Tab. 6), which is significantly below the acceptable limit of 1 Hz , considered necessary for safe detector operation.

Contribution	Rate (Hz)
$\beta\beta 2\nu$	0.03
Composite radioactivity	5.8×10^{-3}
External gammas	1.2×10^{-3}
External neutrons	5×10^{-4}
Radon	0.02
Cosmogenic background	0.015
^{40}K	0.12
Total	0.19

Table 6 Expected event rates in the detector for various contributions.

10 Sensitivity results

The experimental sensitivity can be computed in terms of a limit on the half-life, assuming complete enrichment of ^{136}Xe . The limit can be expressed as:

$$T_{1/2}^{0v} > \ln(2)\epsilon \frac{N_A m}{M} \frac{t}{S_{up}}, \quad (3)$$

where ϵ is the signal efficiency, N_A is Avogadro's number, M is the molar mass of xenon in grams, t is the exposure in years, and m is the active mass of xenon in grams. The signal upper limit, S_{up} , can be computed using a Bayesian upper limit for a Poisson parameter with a uniform prior probability density function (p.d.f.), as explained in Ref. [29]:

$$S_{up} = \frac{1}{2} F_{\chi^2}^{-1}[p, 2(n+1)] - b, \quad (4)$$

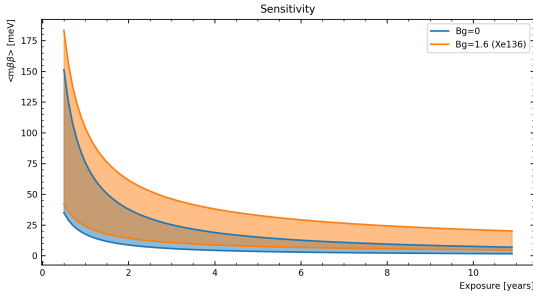


Fig. 13 Expected limits for $\langle m_{\beta\beta} \rangle$ at 90% C.L. for zero background (blue region) and for an expected background of 1.6 events per year (orange band). The width of the band represents the uncertainty in the nuclear matrix elements.

where $F_{\chi^2}^{-1}$ is the quantile of the χ^2 distribution (*i.e.* the inverse of the cumulative distribution), b the expected background, and n the number of observed events. The quantity p is defined as:

$$p = 1 - \alpha(1 - F_{\chi^2}[2b, 2(n+1)]), \quad (5)$$

where F_{χ^2} is the cumulative χ^2 distribution, and $(1-\alpha)$ is the confidence level.

This sensitivity is applicable regardless of the experimental background; however, in the case of a background-free experiment, S_{up} is constant, and the limits depend linearly on the exposure. This is not true for an experiment with background present: the background also increases with exposure (and therefore S_{up}), resulting in a sensitivity dependence that is proportional to the square root of the exposure under the Gaussian description of background fluctuations. The results for different background values can be seen in Fig. 12. With the nominal expected background, a sensitivity on $T_{1/2}^{0\nu}$ of 1.1×10^{27} years can be achieved in 5 years of data taking (1.7×10^{27} years in 10 years of data taking). It is clear that the sensitivity is dominated by the background from the composite material, and to improve it, efforts must be undertaken to develop a thinner vessel that withstands the operating pressure of 40 bars, or one with reduced radioactivity.

The lifetime is related to the effective Majorana mass $\langle m_{\beta\beta} \rangle$ by the following formula:

$$\frac{1}{T_{1/2}^{0\nu}} = G^{0\nu} |M^{0\nu}|^2 \langle m_{\beta\beta} \rangle^2, \quad (6)$$

where $G^{0\nu}$ represents the phase space factor and $M^{0\nu}$ is the matrix element. Using the values from Ref. [42] and the references therein, the limit on $\langle m_{\beta\beta} \rangle$ was computed for zero background, and the current estimate is shown in Fig. 13. Considering the expected background, the limit on $\langle m_{\beta\beta} \rangle$ lies in the range of 7 meV to 33 meV after 5 years, which is reduced to 5 meV to 21 meV if data collection over 10 years is considered.

11 R2D2 in the worldwide panorama

Depending on the final background, the R2D2 proposed detector could completely rule out the inverted mass hierarchy region and begin to address part of the normal one. The performance of the proposed experiment can be compared with future multi-ton experiments. In particular, the following experiments were considered: nEXO [34], LEGEND1000 [43, 44], and CUPID [45]. As shown in Fig. 14, the performance of R2D2 is comparable to that of future proposed experiments and could be even better if zero background is achieved. A reduction of the external gamma component (0.1 events per year) is relatively straightforward, as it depends solely on shielding, whereas the ultimate background arises from composite radioactivity (1.3 events per year) and radon contamination (0.2 events per year). As previously explained, a radioactivity level of $10 \mu\text{Bq/kg}$ is considered in the present study, but efforts are ongoing to potentially reduce this value.

Another point of comparison could be costs and timescale. The timescale is nearly identical for all next-generation experiments, which aim to yield final results around 2040. In this context, R2D2 could be timely, as final results could be expected around 2040 if the program is fully funded and data collection commences in 2030. The cost of the detector is exceptionally low, making R2D2 more than an order of magnitude cheaper than any other future proposed experiment. Furthermore, no cryogenic infrastructure is needed, and the power consumption is minimal, reducing the environmental impact.

Last but not least, given their cost, this type of detector could be deployed in pairs: one filled with natural xenon and the other with ^{136}Xe . Another advantage could lie in the simultaneous deployment of these duplicates in different underground laboratories. This strategy would allow for differential measurements of signal and noise, providing the opportunity to gain a more comprehensive understanding of experimental observations. Coupled with the ability to vary the nature of the medium (*i.e.* Ar or Xe in the adjustment phase), the isotopic content of the gas (natural Xe or ^{136}Xe in the working phase), or to modulate the pressure (up to 50 bars), the proposed scenario could offer valuable redundancies to verify any potential evidence of signals.

Acknowledgements The authors would like to express their gratitude for the support received from various funding sources that contributed to this research. The R&D funding from IN2P3 provided essential resources for the development of the project. Additionally, the OWEN grant from Bordeaux University contributed to the development of low noise electronics. Grants from SUBATECH significantly contributed to the advancement of the research objectives. The authors also acknowledge the use of the computing cluster at the CC Lyon of IN2P3, which was invaluable for the computational aspects of this work.

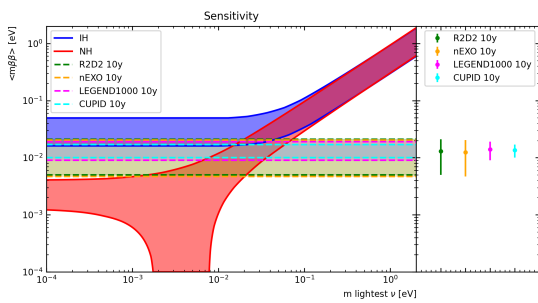


Fig. 14 Expected limits for $\langle m_{\beta\beta} \rangle$ at 90% C.L. for various experiments.

References

- D. Bodeker and W. Buchmuller, *Rev. Mod. Phys.* **93**(3), 035004 (2021). DOI 10.1103/RevModPhys.93.035004
- M. Agostini, G. Benato, J. A. Detwiler, J. Menéndez, and F. Vissani, *Rev. Mod. Phys.* **95**(2), 025002 (2023). DOI 10.1103/RevModPhys.95.025002
- S. Dell’Oro, S. Marcocci, M. Viel, and F. Vissani, *Adv. High Energy Phys.* **2016**, 2162659 (2016). DOI 10.1155/2016/2162659
- N. Burlac and G. Salamanna, *Nucl. Instrum. Meth. A* **1048**, 167943 (2023). DOI 10.1016/j.nima.2022.167943
- I. Nutini et al., *Int. J. Mod. Phys. A* **37**(07), 2240014 (2022). DOI 10.1142/S0217751X22400140
- J. B. Albert et al., *Phys. Rev. C* **97**(6), 065503 (2018). DOI 10.1103/PhysRevC.97.065503
- R. Bouet et al., *JINST* **16**(03), P03012 (2021). DOI 10.1088/1748-0221/16/03/P03012
- R. Bouet et al., *JINST* **18**(10), T10001 (2023). DOI 10.1088/1748-0221/18/10/T10001
- P. Lautridou, *J. Phys. Conf. Ser.* **2502**(1), 012006 (2023). DOI 10.1088/1742-6596/2502/1/012006
- R. Bouet et al., *JINST* **18**(03), P03031 (2023). DOI 10.1088/1748-0221/18/03/P03031
- R. Bouet et al., *Eur. Phys. J. C* **84**, 512 (2024). DOI 10.1140/epjc/s10052-024-12864-w
- IRT Jules Verne, <https://www.irt-jules-verne.fr>
- A. Meregaglia et al., *JINST* **13**(01), P01009 (2018). DOI 10.1088/1748-0221/13/01/P01009
- F. Piquemal, Talk at 11th international symposium on Large TPCs for low-energy rare event detection (2023)
- MAHYTEC, <https://www.mahytec.com/fr/>
- J. Busto, Y. Gonin, J. M. Vuilleumier, F. Hubert, and P. Hubert, *Nucl. Instrum. Meth. A* **492**, 35 (2002). DOI 10.1016/S0168-9002(02)01280-9
- E. Armengaud et al., *JINST* **12**(08), P08010 (2017). DOI 10.1088/1748-0221/12/08/P08010
- G. Plante, E. Aprile, J. Howlett, and Y. Zhang, *Eur. Phys. J. C* **82**(10), 860 (2022). DOI 10.1140/epjc/s10052-022-10832-w
- D. Y. Akimov et al., *Instrum. Exp. Tech.* **60**(6), 782 (2017). DOI 10.1134/S002044121705013X
- F. LePort et al., *Rev. Sci. Instrum.* **82**, 105114 (2011). DOI 10.1063/1.3653391
- S. Agostinelli et al., *Nucl. Instrum. Meth. A* **506**, 250 (2003). DOI 10.1016/S0168-9002(03)01368-8
- V. Alvarez et al., *JINST* **8**, P05025 (2013). DOI 10.1088/1748-0221/8/05/P05025
- R. Veenhof, *Conf. Proc. C* **9306149**, 66 (1993)
- R. Bouet et al., *Nucl. Instrum. Meth. A* **1028**, 166382 (2022). DOI 10.1016/j.nima.2022.166382
- J. Cussonneau et al., *Nucl. Instrum. Meth. A* **492**, 26 (2002). DOI 10.1016/S0168-9002(02)01275-5
- D. Nygren, *J. Phys. Conf. Ser.* **309**, 012006 (2011). DOI 10.1088/1742-6596/309/1/012006
- A. Bolotnikov and B. Ramsey, *Nucl. Instrum. Meth. A* **396**(3), 360 (1997). DOI [https://doi.org/10.1016/S0168-9002\(97\)00784-5](https://doi.org/10.1016/S0168-9002(97)00784-5)
- J. Kotila and F. Iachello, *Phys. Rev. C* **85**, 034316 (2012). DOI 10.1103/PhysRevC.85.034316
- R. L. Workman et al., *PTEP* **2022**, 083C01 (2022). DOI 10.1093/ptep/ptac097
- H. Ohsumi et al., *Nucl. Instrum. Meth. A* **482**, 832 (2002). DOI 10.1016/S0168-9002(01)01866-6
- G. J. Feldman and R. D. Cousins, *Phys. Rev. D* **57**, 3873 (1998). DOI 10.1103/PhysRevD.57.3873
- D. Mei and A. Hime, *Phys. Rev. D* **73**, 053004 (2006). DOI 10.1103/PhysRevD.73.053004
- M. Murra, D. Schulte, C. Huhmann, and C. Weinheimer, *Eur. Phys. J. C* **82**(12), 1104 (2022). DOI 10.1140/epjc/s10052-022-11001-9
- G. Adhikari et al., *J. Phys. G* **49**(1), 015104 (2022). DOI 10.1088/1361-6471/ac3631
- O. Veselska, O. Llido, M.-C. Piro, S. Vaidya, S. Kuznicki, and J. Busto, *Progress of Theoretical and Experimental Physics* **2024**(2), 023C01 (2023). DOI 10.1093/ptep/ptad160
- E. Aprile et al., *Eur. Phys. J. C* **84**(8), 784 (2024). DOI 10.1140/epjc/s10052-024-12982-5
- X. Lu et al., *Chin. Phys. C* **48**(9), 091001 (2024). DOI 10.1088/1674-1137/ad582a
- J. B. Albert et al., *JCAP* **04**, 029 (2016). DOI 10.1088/1475-7516/2016/04/029
- M. Adrover et al., *Eur. Phys. J. C* **84**(1), 88 (2024). DOI 10.1140/epjc/s10052-023-12298-w
- L. Rogers et al., *J. Phys. G* **47**(7), 075001 (2020). DOI 10.1088/1361-6471/ab8915
- C. Cuesta et al., *Int. J. Mod. Phys. A* **29**, 1443010 (2014). DOI 10.1142/S0217751X14430106
- S. Abe et al., *Phys. Rev. Lett.* **130**(5), 051801 (2023). DOI 10.1103/PhysRevLett.130.051801
- N. Abgrall et al., (2021). ArXiv:2107.11462

44. LEGEND1000, <https://legend-exp.org/science/legend-pathway/legend-1000>
45. A. Armatol et al., (2022). ArXiv:2203.08386